Entanglement Network of the Polypropylene/Polyamide Interface. 3. Deformation to Fracture

Andreas F. Terzis,[†] Doros N. Theodorou,[*,‡,§] and Alexander Stroeks[||]

Department of Physics, University of Patras, GR 26500 Patras, Greece; Department of Chemical Engineering, University of Patras, GR 26500 Patras, Greece; Institute of Chemical Engineering and High-Temperature Chemical Processes, GR 26500 Patras, Greece; and DSM Research, P.O. Box 18, 6160 MD Geleen, The Netherlands

Received April 23, 2001; Revised Manuscript Received September 5, 2001

ABSTRACT: Recently (*Macromolecules* **2000**, *33*, 1385, 1396), we have proposed a novel algorithm for generating entanglement network specimens of interfacial polymeric systems. The specimens are created by sampling the configurational distribution functions derived from a self-consistent mean field lattice model. Although overstretched strands can be relaxed by a Monte Carlo (MC) method, the specimens generated are not in detailed mechanical equilibrium. In this paper, we develop a method for relaxing the network with respect to its density distribution, and thereby imposing the condition of mechanical equilibrium, without changing the network topology. Our method rests on minimizing a free energy function characterizing the network, with respect to the coordinates of all entanglement points and chain ends. Contributions to the free energy include (a) the elastic energy due to stretching of the chain strands and (b) the free energy due to the repulsive and attractive (cohesive) interactions between segments. To calculate the interaction energy, a simple cubic grid is superimposed on the network. The repulsive interactions are calculated within each grid cell. The attractive interactions are calculated from contributions between cells and within each cell. We first apply the free energy minimization procedure to a simple system (bulk polypropylene) and obtain results which agree satisfactorily with experimental data and serve as a basis for parametrizing the interaction model. The free energy minimization is then applied to mechanically relax computer specimens of a polypropylene/polyamide6 (PP/PA6) interfacial system, strengthened by PP chains grafted onto the PA6 surface. The fully relaxed networks serve as a starting point for the mesoscopic simulation of fracture phenomena, caused by the application of tensile stress perpendicular to the interface. The network is deformed at a constant strain rate and the network topology evolves according to elementary mechanical processes of chain scission, chain slippage, disentanglement, and reentanglement. Chain slippage across an entanglement point occurs according to a Zhurkov activated rate equation with parameters derived from viscosity data. Each cycle of the kinetic MC algorithm used to track the deformation process consists of the imposition of a small incremental strain on the network, relaxation to mechanical equilibrium, introduction of the micromechanical processes mentioned above, and again relaxation to mechanical equilibrium. The MC cycles are repeated until fracture occurs. Results of the fracture experiments confirm the assertion, previously founded on structural grounds, that optimal adhesion in the PP/PA6 system examined is achieved for a relatively low surface grafting density of 0.1 chains/nm^2.

1. Introduction

This work is the continuation of an effort[1,2] to develop theoretical and computer simulation tools for predicting the structure and mechanical properties of immiscible polymer/polymer interfaces compatibilized by adding, or forming in situ with appropriate chemical reactions, a diblock copolymer in which each block is miscible with one of the two homopolymers.[3,4] We focus on the PP/PA6 system, which has been the subject of several experimental studies,[4−6] compatibilized with the reaction product between PP-*g*-MA (maleic anhydride−functionalized PP) and PA6.

In our previous work,[2] we have developed an algorithm in order to generate coarse-grained entanglement networks, representative of this interfacial system. This coarse-grained representation is based on the idea that the ultimate mechanical properties of polymeric systems are directly related to entanglements among chains.

To generate networks representative of the real PP/PA6 interfacial system, we have respected the information provided by experimental data.[5,6] We have considered a crystalline PA6 matrix (i.e., an equivalent "solid" substrate) on which the PP chains of the compatibilizer are terminally grafted, extending into a bulk PP phase (i.e., a collection of free PP chains).

Adopting a coarse-grained (mesoscopic) model is dictated by limitations in computer time for tracking the length scales and time scales relevant to fracture phenomena. Actually, two levels of coarse-graining are utilized. First, a fully occupied lattice is used to represent the system of interest, the structure of the lattice model being determined by a self-consistent field (SCF) theory. Next, the structural information derived from the SCF theory is used to build an entanglement network model in continuous three-dimensional space. In the lattice model, each chain species is viewed as a sequence of Flory segments, each segment occupying exactly one site. The Flory segment size is determined

* To whom correspondence should be addressed at the University of Patras. Telephone: +3061−997398. Fax: +3061−993255. E-mail: doros@sequoia.chemeng.upatras.gr.
[†] Department of Physics, University of Patras.
[‡] Department of Chemical Engineering, University of Patras.
[§] Institute of Chemical Engineering and High-Temperature Chemical Processes.
[||] DSM Research.

10.1021/ma010691z CCC: $22.00
Published on Web 12/13/2001

from the mass density and contour length of the homopolymer species present, as detailed in ref 1. Chain stiffness is also faithfully represented by introducing appropriate intermolecular energetics. In ref 2, using the one-dimensional information provided by the SCF theory as a starting point, we developed an algorithm in order to generate large, three-dimensional networks representative of the interfacial region. In the network, a chain is represented as a sequence of two ends and a set of intermediate nodal points, the latter participating in entanglements. Two chains come together at an entanglement point. Chain ends and entanglement points are referred to collectively as nodes of the network. Our construction results in a set of nodes for each chain, where each node has a specific contour position along the chain, positional vector in three-dimensional space, and pairing with another node if it participates in an entanglement. The piece of chain between two nodes is referred to as a strand. The generated networks have been relaxed with regard to stretching of the strands (see Monte Carlo methodology developed in ref 2), but not with regard to the density distribution; thus, they are likely to incorporate large unbalanced stresses associated with excluded volume and cohesive interactions. To relax the large density fluctuations and bring the system to mechanical equilibrium (i.e., a state in which the total force at every node is zero), we have to minimize (locally) an appropriately formulated Helmholtz free energy with respect to all nodal positions.

In this work, we develop a methodology to estimate the free energy of the coarse-grained network models. Conformational and nonbonded interaction contributions are taken into account. The conformational part comes from the stretched strands. The nonbonded interaction contribution is divided into an attractive part (van der Waals forces) and a repulsive part (excluded volume interactions). To estimate these contributions, the local segment density is needed. Once the free energy function is known, mechanical equilibrium is imposed by minimization of the free energy with respect to the positions of all nodes.

Deformation experiments are performed on the network at a constant strain rate by a kinetic Monte Carlo (KMC) scheme, inspired by the one developed in ref 7. In the course of a simulation of deformation to fracture, the topology of the entanglement network changes through the introduction of elementary events (e.g., slippage of a chain past an entanglement point, chain rupture) governed by rate expressions and rules which are based on the reptation picture of polymer dynamics. KMC simulations of simplified two-dimensional network models have proved quite successful for addressing the terminal properties of semicrystalline polymers in the bulk,[7] thus providing justification for the use of representations cast in terms of localized entanglement points for modeling the large-scale deformation and fracture of dense systems of interpenetrating chains. Here, a much more detailed three-dimensional scheme is developed, in which excluded volume interactions are accounted for explicitly, mechanical equilibrium is imposed throughout the deformation process, and no a priori imposition of the Poisson ratio is required.

Typical sizes of the network system generated and deformed in this work are 0.1 μm on each side. The number of chains can be as high as 20 000 and the number of entanglement points as high as 130 000. The simulation of larger systems is well possible with currently available parallel computational resources.

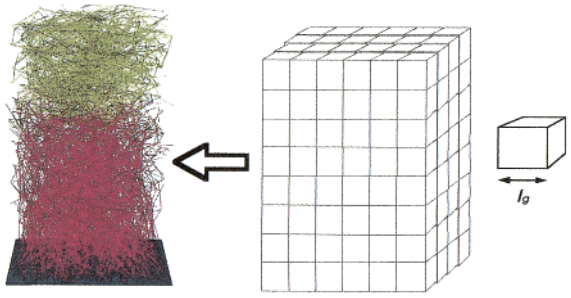

Figure 1. Simple cubic grid superimposed on the network specimen.

2. Network Free Energy

General Assumptions. Our network consists of chains, represented by specific points (nodes, i.e., entanglements or ends) along their contour. All nodal points have specific spatial positions. The initial contour length between consecutive entanglement points on the same chain is specified by the entanglement molecular weight M_e (in this work, as in ref 2, $M_e = 6$ kg/mol). Note that, in the PP/PA6 interfacial system, the value for M_e could be different, as all grafted and some free chains are more ordered along the direction perpendicular to the interface. However, as a first approximation, we use the bulk value because of lack of an alternative approach. To relax the network without changing its topology and thereby impose the condition of mechanical equilibrium at the current topology, we need to minimize the network free energy with respect to the coordinates of the entanglement points and chain ends. Contributions to the free energy include (a) the entropic free energy due to stretching of the chain strands and (b) the free energy due to the repulsive (excluded volume) and attractive (cohesive) interactions between segments. To calculate the interaction energy, a simple cubic grid is superimposed on the network (see Figure 1). The grid, which remains unchanged throughout all simulations described here, partitions the network into small cubic regions or cells. The edge length, l_g, of each cell is commensurate with the distance between entanglements in three-dimensional space. The repulsive interactions are calculated within each grid cell. The attractive interactions are calculated from contributions between cells and within each cell.

Initially, to test our method, we have applied the free energy minimization procedure to a network representative of bulk isotactic PP at room temperature. With the parameters we chose for the representation of nonbonded interactions (see below), the results were found to agree satisfactorily with experimental values of the mass density, cohesive energy density, and bulk modulus. Then, the free energy minimization procedure was applied to mechanically relax the more complex PP/PA6 interfacial system.

Network Density Distribution. The local density is calculated in each cell of the simple cubic grid of spacing l_g that is superimposed on the network. Each strand of the network contributes to the local density in a way which depends on the number of Flory (or Kuhn) segments in the strand and on the spatial positions of the ends of the strand.

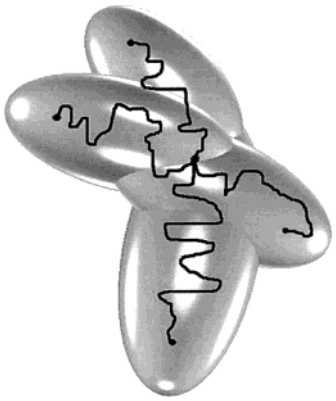

Figure 2. Strand "segment density clouds". The segment density inside each cell is calculated by superposition of segment clouds.

Thus, the number density of monomers in a cell indexed by W is given by a sum of contributions to that cell from each strand of the network (see Figures 2, 3)

$$\rho_W = \int \mathrm{d}\vec{R} \sum_{i<} \sum_{j} c_{ij} \rho\left(\vec{R} - \frac{\vec{R}_i + \vec{R}_j}{2}, |\vec{R}_j - \vec{R}_i|, n_{\mathrm{K}_{ij}}\right) \times \left[\Theta\left(\frac{l_\mathrm{g}}{2} - |R_x - R_{xW}|\right) \Theta\left(\frac{l_\mathrm{g}}{2} - |R_y - R_{yW}|\right) \times \Theta\left(\frac{l_\mathrm{g}}{2} - |R_z - R_{zW}|\right)\right] \quad (1)$$

where the sums are over all nodes (entanglement points and ends) i and j and $\vec{R}_W$ is the position vector of the center of the cell. The length of the strand between nodes i and j is specified by $n_{\mathrm{K}_{ij}}$, the number of Kuhn segments. The connectivity factor c_{ij} is defined as

$$c_{ij} = \begin{cases} n^{\mathrm{mK}} & \text{if nodes } i \text{ and } j \text{ are connected by a strand} \\ 0 & \text{otherwise} \end{cases} \quad (2)$$

where n^{mK} is the number of monomers per Kuhn segment. In the above expression, Θ is the Heaviside function.

The local strand segment density distributions $\rho(\vec{R} - (\vec{R}_i + \vec{R}_j)/2, |\vec{R}_j - \vec{R}_i|, n_{\mathrm{K}_{ij}})$ are measured in Kuhn statistical units (i.e. units that follow a random walk statistics) per unit volume. They are conveniently expressed in terms of a reduced strand density $\tilde{\rho}$ as $\rho = n_{\mathrm{K}_{ij}} \tilde{\rho} / {l_\mathrm{K}}^3$. ρ is the density (in Kuhn segments per unit volume) in the region specified by the position vector $\vec{R}$, due to a strand of length $n_{\mathrm{K}_{ij}}$ Kuhn segments, given that the start of the Kuhn segment 1 and the end of the Kuhn segment $n_{\mathrm{K}_{ij}}$ are fixed at positions $\vec{R}_i$ and $\vec{R}_j$, respectively (see Figure 3).

Local Density of Segments. In eq 1, the cell density ρ_W is expressed in terms of a reduced segment density distribution $\tilde{\rho}$ of a strand tethered at both ends. Fischel et al.[8] have derived the exact solution for the end-to-end distance distribution of freely jointed chain strands and applied it to estimate the distributions of the intermediate segments of the strands. Although the exact solution is known, its implementation in the problem studied here is computationally very expensive. For some regions (for example, short distance between the nodes and large number of Kuhn segments), it is usually preferable to use approximate solutions (i.e., the corresponding solution for a Gaussian chain strand), which are less accurate (usually with few percent error) but much less expensive computationally. In the present work, we perform a numerical (very accurate) calculation of the local density distributions of tethered freely jointed chains. In this calculation, a tethered strand is represented as a sequence of bonds, the length of each bond being equal to the size of a Kuhn statistical unit. At fixed spatial distance between the two terminal nodes and with known number of Kuhn segments in the strand, we use Monte Carlo sampling in order numerically to compute and tabulate the segment density. We start the Monte Carlo sampling with an equilateral V shape for the strands (each side of the V connecting a tethered end to a point on the perpendicular bisector of the line segment connecting the tethered ends). "Pivot" MC moves are used,[9,10] which entail rotations of randomly chosen parts of the strand about the axis connecting their terminal segments. The rotation angle is chosen randomly from 0 to 2π. The pretabulation of the density is performed for a strand with number of Kuhn segments determined by the average molecular weight between entanglements (i.e., 34 Kuhn segments). The values used for the end to end distance ranged from zero to full extension, with a constant interval between successive values; results were pretabulated for a total of 101 end-to-end distances. For intermediate values we have proved that a linear interpolation is an excellent approximation.

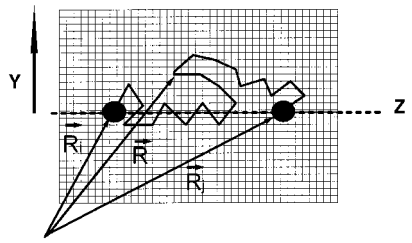

Figure 3. Local coordinate system around a strand. The grid shown is the one over which we perform the pretabulation of the local density.

Because of symmetry of the distribution of tethered chain segments about the axis of the end-to-end vector, only two spatial coordinates are necessary in the pretabulation: z, along to the end-to-end vector, and y, normal to it (see Figure 3). To find the density of a strand at position $\vec{R}$ in space, with its first segment beginning at $\vec{R}_i$ and its last segment ending at $\vec{R}_j$, the corresponding z and y values can be determined using the dot ($\cdot$) and cross ($\times$) products of vectors (where the origin for z and y coordinates is the position of the midpoint of the distance between the tethered ends):

$$z = \frac{\left(\vec{R} - \frac{\vec{R}_i + \vec{R}_j}{2}\right) \cdot (\vec{R}_j - \vec{R}_i)}{|\vec{R}_j - \vec{R}_i|} \quad (3)$$

$$y = \frac{\left|\left(\vec{R} - \frac{\vec{R}_i + \vec{R}_j}{2}\right) \times (\vec{R}_j - \vec{R}_i)\right|}{|\vec{R}_j - \vec{R}_i|}$$

Moreover, we have shown that, for any number of segments, a Gaussian scaling of the density with respect to the distance between the tethered ends is valid for

extensions up to some "upper limit" value, which depends on the number of segments. For large number of segments in the strand and small distance between the tethered ends, this Gaussian scaling is confirmed analytically.[8,11] A linear scaling of the density with respect to the distance between the tethered ends is valid for extensions larger than this "upper limit" value. Actually, for a given number of segments at extension exactly corresponding to the "upper limit" value, Gaussian and linear scaling are equally well applicable. By linear scaling we mean that the reduced strand density $\tilde{\rho}$ at position (z, y) of a tethered strand of n^a segments with ends at spatial distance $R_{12}{}^a$ from each other is the same as $\tilde{\rho}$ of a strand of n^b segments with ends at spatial distance $R_{12}{}^b = (n^b/n^a)R_{12}{}^a$ at position $[(n^b/n^a)z, (n^b/n^a)y]$. By Gaussian scaling, on the other hand, we mean that $\tilde{\rho}(z, y)$ of a strand of n^a segments with ends a distance $R_{12}{}^a$ apart is the same as $\tilde{\rho}(z, y)$ of a strand of n^b segments with spatial distance between the ends $R_{12}{}^b = \sqrt{(n^b/n^a)}\ R_{12}{}^a$ at position $(\sqrt{(n^b/n^a)}z, \sqrt{(n^b/n^a)}y)$. Our studies have shown that special care is needed for strands consisting of a very small number of segments. In this case, however, as we have to distribute in space a very small number of segments, the results are *practically* very similar, no matter what scaling is adopted.

In our calculations, it is the reduced strand density $\tilde{\rho}$ that is pretabulated as a function of scaled z and y coordinates, with parameter a nondimensionalized strand end-to-end distance α:

$$\tilde{\rho}\left(\frac{z}{l_K n_{K_{ij}}{}^h}, \frac{y}{l_K n_{K_{ij}}{}^h}, \alpha \equiv \frac{|\vec{R}_j - \vec{R}_i|}{l_K n_{K_{ij}}{}^h}\right)$$

Here $h = 1$ for linear scaling and $h = {}^1/_2$ for Gaussian scaling and $|\vec{R}_j - \vec{R}_i|/(l_K n_{K_{ij}})$ takes values from 0.00 to 1.00 with step 0.01.

The local Kuhn segment density at $\vec{R}$ due to the strand ij is calculated immediately, once the reduced strand density is known:

$$\rho\left(\vec{R} - \frac{\vec{R}_i + \vec{R}_j}{2}, |\vec{R}_j - \vec{R}_i|, n_{K_{ij}}\right) = \tilde{\rho}\left(\frac{z}{l_K n_{K_{ij}}{}^h}, \frac{y}{l_K n_{K_{ij}}{}^h}, \alpha\right)\frac{n_{K_{ij}}}{l_K{}^3} \tag{4}$$

Free Energy Calculation. The free energy of the network has three contributions: (1) the elastic energy of the stretched strands; (2) the attractive interactions between segments; and (3) the repulsive interactions between segments:

$$A = \sum_{\substack{i<j \\ i,j \text{ connected}}} A_{ij}{}^{\text{entropy spring}} + \sum_W A_W{}^{\text{rep}} + \sum_W A_W{}^{\text{attr}} + \sum_{\substack{W<V \\ W,V \text{ neighbors}}} A_{W,V}{}^{\text{attr}} \tag{5}$$

where i and j represent the nodes (connected by a strand) and the indices W and V specify the cells of the grid used for spatial partitioning of the network.

The repulsive interactions ($A_W{}^{\text{rep}}$) act between segments within a grid cell. The attractive interactions act between segments in the same cell ($A_W{}^{\text{attr}}$) and also between segments in adjacent cells ($A_{W,V}{}^{\text{attr}}$).

Elastic Interactions. The elastic force between connected nodes arises due to the retractive force acting to resist the stretching of a strand. This force originates in the decrease in entropy of a stretched polymer strand. The Gaussian approximation can be used for most extensions.[8] In this approximation, the force on node i due to its connection to node j is[12]

$$\vec{F}_{ij}{}^{\text{entropy string}} \equiv -\nabla_{\vec{R}_{ij}} A_{ij}{}^{\text{entropy spring}} = 3k_B T \frac{\vec{R}_{ji}}{n_{K_{ij}} l_K{}^2} \tag{6}$$

where $\vec{R}_{ij} \equiv \vec{R}_i - \vec{R}_j$.

For higher extensions the inverse Langevin approximation or an even more accurate functional dependence, computed by simulation, could be used. However, as the contribution of the elastic energy to the total free energy is minor, such computationally more expensive expressions were not implemented in the present study. The elastic force depends on the coordinates of the nodes, but it does not depend on the local network density.

The corresponding expression for the free energy of an entropy spring is

$$A_{ij}{}^{\text{entropic spring}} = \frac{3}{2} k_B T \frac{(\vec{R}_{ij} \cdot \vec{R}_{ij})}{n_{K_{ij}} l_K{}^2} \tag{7}$$

Repulsive Interactions. The repulsive force ensures that the density distribution is such that segments do not overlap. The simplest approximation is to identify each segment with a hard sphere. The best known equation of state of the hard-sphere fluid is the Carnahan−Starling equation of state, $\beta P/\rho = (1 + \eta + \eta^2 - \eta^3)/(1 - \eta)^3$, with $\beta \equiv 1/k_B T$, P being the pressure, ρ the number density, and η the packing fraction.

This equation of state provides an excellent fit to the results of computer simulations over the entire *fluid* range.

From this expression, a simple form is obtained for the Helmholtz free energy in cell W:

$$\frac{\beta A_W{}^{\text{rep}}}{N} = \ln(\rho_W \Lambda^3) - 1 + \frac{(4\eta_W - 3\eta_W{}^2)}{(1 - \eta_W)^2} \tag{8}$$

in which $\eta_W = (\pi/6)\rho_W d_{HS}{}^3$ is the packing fraction, ρ_W the monomer number density, and d_{HS} the hard sphere diameter. The first three terms in the free energy expression comprise the contribution from an ideal gas of segments. In this expression, $\Lambda \equiv [h^2/(2\pi k_B T m)]^{1/2}$ is the thermal wavelength of a segment, h is Planck's constant, and m is the mass of the segment treated as a hard sphere. In dealing with repulsive and attractive interactions, we take the chemical monomer as the unit segment. In this case, the diameter d_{HS} of the hard sphere representation of the PP monomer was treated as a parameter, determined by fitting the mass density, the cohesive energy density, and the bulk modulus of bulk PP.

There are two terms in eq 8 that could cause problems in our simulations. One is the term from the ideal gas contribution, $\ln(\rho_W \Lambda^3) - 1$. For very low densities, this

term diverges (i.e., empty cells give a huge negative contribution). To avoid unphysical complications from the almost empty cells at the edges of our sample, we introduce a cutoff density. Below this cutoff there is no contribution to the free energy. The other problem has to do with the fact that, if used for packing fraction larger than unity, eq 8 gives a free energy that is a decreasing function of the packing fraction (last term $(4\eta_W - 3\eta_W^2)/(1 - \eta_W)^2$). Since such unphysically high values of η_W may be encountered in the initial stages of our minimization, we need to correct for this by assuming a reasonable continuation of the free energy function. The simplest solution, adopted here, is to assume that the free energy has a constant value for packing fractions greater than unity [we use $A_W^{rep}(\eta_W = 0.99999)$ as this constant value].

Attractive Interactions. The attractive interactions add to elastic spring forces to increase the cohesion of the material. Since attractive forces are weaker and longer range than repulsive forces, a mean field representation of the density of segments within a lattice cell provides a sufficient level of approximation. The attractive interaction potential scales inversely with the sixth power of the separation distance (London dispersion forces). The net attractive interaction potential between the segments of cells W and V, centered at $\vec{R}_W$ and $\vec{R}_V$ respectively, is calculated by integration of the pair interactions between volume elements in the two cells

$$A_{W,V}^{attr} = -\rho_W\rho_V\int_{R_{xW}-\frac{l_g}{2}}^{R_{xW}+\frac{l_g}{2}}\int_{R_{yW}-\frac{l_g}{2}}^{R_{yW}+\frac{l_g}{2}}\int_{R_{zW}-\frac{l_g}{2}}^{R_{zW}+\frac{l_g}{2}}\int_{R_{xV}-\frac{l_g}{2}}^{R_{xV}+\frac{l_g}{2}}\int_{R_{yV}-\frac{l_g}{2}}^{R_{yV}+\frac{l_g}{2}}\int_{R_{zV}-\frac{l_g}{2}}^{R_{zV}+\frac{l_g}{2}} 4\epsilon\Theta(|\vec{R}'_W - \vec{R}'_V| - d_{HS})\left(\frac{\sigma_{LJ}}{|\vec{R}'_W - \vec{R}'_V|}\right)^6 d\vec{R}'_W\, d\vec{R}'_V \quad (9)$$

where ϵ and σ_{LJ} are Lennard-Jones (LJ) parameters. The Θ-function expresses the fact that segments in adjacent lattice cells never get closer than the hard core diameter.

As the density is constant within each cell, the integral depends on the distance between the cell centers and on the relative arrangement of the cells.

Consequently, the integration may be performed numerically and tabulated for each kind of cell arrangement as

$$I_{W,V} = -4\epsilon\sigma_{LJ}^6\int_{R_{xW}-\frac{l_g}{2}}^{R_{xW}+\frac{l_g}{2}}\int_{R_{yW}-\frac{l_g}{2}}^{R_{yW}+\frac{l_g}{2}}\int_{R_{zW}-\frac{l_g}{2}}^{R_{zW}+\frac{l_g}{2}}\int_{R_{xV}-\frac{l_g}{2}}^{R_{xV}+\frac{l_g}{2}}\int_{R_{yV}-\frac{l_g}{2}}^{R_{yV}+\frac{l_g}{2}}\int_{R_{zV}-\frac{l_g}{2}}^{R_{zV}+\frac{l_g}{2}} \left(\frac{1}{|\vec{R}'_W - \vec{R}'_V|}\right)^6 \Theta(|\vec{R}'_W - \vec{R}'_V| - d_{HS})\, d\vec{R}'_W\, d\vec{R}'_V \quad (10)$$

This integral depends only on $|\vec{R}_W - \vec{R}_V|/\sigma_{LJ}$, d_{HS}/σ_{LJ}, and l_g/σ_{LJ}. The result of such an integration is usually called a Hamaker constant in colloidal chemistry.[13] For first neighbor cubes there are three types of arrangements: sharing a face (distance between cell centers equal to the length of each edge, l_g), sharing an edge (distance between cells equal to $\sqrt{2}l_g$) and sharing a corner (distance between cells equal to $\sqrt{3}l_g$).

For attractive interactions between segments belonging to the same cell, the same procedure can be used; again the interactions must be constrained, such that the two volume elements (within the same cell) are never closer than d_{HS}. These integrations may be performed numerically and tabulated as I_W (same for all cells), where

$$I_W = -4\epsilon\sigma_{LJ}^6 \times \int_{R_{xW}-\frac{l_g}{2}}^{R_{xW}+\frac{l_g}{2}}\int_{R_{yW}-\frac{l_g}{2}}^{R_{yW}+\frac{l_g}{2}}\int_{R_{zW}-\frac{l_g}{2}}^{R_{zW}+\frac{l_g}{2}}\int_{R_{xW}-\frac{l_g}{2}}^{R_{xW}+\frac{l_g}{2}}\int_{R_{yW}-\frac{l_g}{2}}^{R_{yW}+\frac{l_g}{2}}\int_{R_{zW}-\frac{l_g}{2}}^{R_{zW}+\frac{l_g}{2}} \left(\frac{1}{|\vec{R}'_W - \vec{R}''_W|}\right)^6 \Theta(|\vec{R}'_W - \vec{R}''_W| - d_{HS})\, d\vec{R}'_W\, d\vec{R}''_W \quad (11)$$

This integral is solely a function of d_{HS}/σ_{LJ} and l_g/σ_{LJ}. Thus, the attractive interactions reduce to the simple form:

$$A^{attr} = \sum_W \rho_W\left[\frac{1}{2}\sum_{V\ \text{neighboring}\ W} I_{W,V}\rho_V + I_W\rho_W\right] \quad (12)$$

One may ask if we could use an integrated version of the repulsive part (which scales inversely with the 12th power of separation distance) of the Lennard-Jones potential to describe repulsive interactions within each cell, as we do for attractions. Exploratory calculations have confirmed what is known from liquid theory, namely that an integration (mean field treatment) of repulsions results in interactions which are not strong enough, and therefore a more explicit treatment of repulsions (incorporated here through our use of the Carnahan−Starling free energy) is necessary.

Minimization of the Free Energy. To relax the network fully, we need to minimize its free energy with respect to the positions of entanglement points and end points. The minimization procedure is driven by the derivative of the free energy with respect to each independent variable (here, the spatial coordinates of entanglements and end points). The minimum corresponds to the vanishing of all derivatives. The numerical estimation of the derivatives by taking finite differences of the free energy is a very time-consuming procedure, as calculation of N partial derivatives requires N calculations of the free energy (N = number of independent variables). We can either try to bypass the calculation of the derivatives by adopting a numerical minimization method where derivatives are not explicitly required, or develop a fast, semianalytical scheme for the numerical estimation of derivatives in a much less expensive way. Minimization methods that do not require the estimation of the derivatives (a prototype being Powell's method[14]), require storage of order N^2. This is so demanding in computer memory that it proved impractical with the computational facilities we had available. The only practical solution based on Powell's method was to partition our network specimens into subdomains, whose free energy is minimized separately. This piecewise minimization has to be repeated several times, switching the domain boundaries to include regions that were not used in past iterations, until any new iteration does not alter the values of calculated physical properties. On the other hand, conjugate gradient methods[14] require storage only of order N, but require partial derivatives. We have developed a semianalytical scheme for obtaining the derivatives in a fast and accurate manner, while calculating the free energy. As mentioned above, the free energy is calculated by means of the pretabulated local densities in the grid cells. Similarly, it is much faster if one calculates the derivatives of the free energy by

means of pretabulated derivatives of the segment densities contributed to the various cells by each chain strand.

The derivative of the free energy with respect to the coordinates of a node i is

$$\frac{\partial A}{\partial \vec{R}_i} \equiv \nabla_{\vec{R}_i} A = \nabla_{\vec{R}_i} A^{\text{entropy spring}} + \nabla_{\vec{R}_i} A^{\text{rep}} + \nabla_{\vec{R}_i} A^{\text{attr}} = \sum_{j \text{ connected } to\ i} \nabla_{\vec{R}_{ij}} A_{ij}^{\text{entropy string}} + \sum_W \frac{\partial A_W^{\text{rep}}}{\partial \rho_W} \nabla_{\vec{R}_i} \rho_W + \sum_W \frac{\partial A_W^{\text{attr}}}{\partial \rho_W} \nabla_{\vec{R}_i} \rho_W + \sum_{\substack{W<V \\ W \text{ neighboring } V}} \left(\frac{\partial A_{W,V}^{\text{attr}}}{\partial \rho_W} \nabla_{\vec{R}_i} \rho_W + \frac{\partial A_{W,V}^{\text{attr}}}{\partial \rho_V} \nabla_{\vec{R}_i} \rho_V \right) \quad (13)$$

From the analytic expressions of the attractive and repulsive contributions to the free energy (eq 8 and eq 12), we readily obtain the derivatives of A^{rep} and A^{attr} with respect to the density (ρ_W) of each cell. Similarly, eq 6 gives us the entropy spring part of the force on i, since the corresponding free energy depends directly on the distance vector $\vec{R}_{ij}$. Therefore, for the calculation of the derivatives of the free energy we need only the gradients of the local densities with respect to the position vectors $\vec{R}_i$. The segment density of each cell is calculated from the contributions of all stands that have part or all of their "density cloud" inside the cell (eq 1, see Figure 2).

It is obvious from eq 1 that, to estimate $\nabla_{\vec{R}_i}\rho_W$, we need the derivatives of the reduced segment density ($\tilde{\rho}$):

$$\nabla_{\vec{R}_i} \tilde{\rho}\left(\frac{z}{l_K n_K^{\text{h}}}, \frac{y}{l_K n_K^{\text{h}}}, \alpha\right) = \left(\frac{\partial \tilde{\rho}}{\partial (z/l_K n_K^{\text{h}})} \nabla_{\vec{R}_i} z + \frac{\partial \tilde{\rho}}{\partial (y/l_K n_K^{\text{h}})} \nabla_{\vec{R}_i} y + \frac{\partial \tilde{\rho}}{\partial \alpha} \nabla_{\vec{R}_i} |\vec{R}_{ij}| \right) \frac{1}{l_K n_K^{\text{h}}} \quad (14)$$

The derivatives of the reduced strand segment density with respect to the scaled variables $z/l_K n_K^{\text{h}}$, $y/l_K n_K^{\text{h}}$ and α are calculated numerically and tabulated. The gradients of z, y, and $|\vec{R}_{ij}|$ with respect to the internodal distance vector are calculated analytically using the geometric relations, eq 3.

Relaxation of Bulk PP Network. To describe realistic bulk PP and PP/PA6 systems, we have to deal with the semicrystallinity of PP. The most accurate way to do this would entail an explicit introduction of the semicrystallinity from the very beginning (i.e., generation of representative model systems containing crystallites).[15] Here we follow a simpler route. In our existing model, we deal with semicrystallinity by "adjusting" the model parameters so as to reproduce the actual properties (density, cohesive energy density, elastic constants, viscosity in the melt state) of isotactic, semicrystalline PP. Model parameters are thus determined by comparison with experimental thermodynamic and deformation data on bulk semicrystalline PP samples.

In our simulation of bulk isotactic PP, we work at room temperature, since all mechanical experiments are performed at room temperature. At this temperature, we have to assign new values to the Flory segments and to the bending energies (relative to those used in our SCF calculations), as both density and stiffness depend on temperature. We estimated the experimental specific volume of PP as an arithmetic average between the specific volume of a fully crystalline PP and of a rubbery amorphous PP (i.e. for a semicrystalline PP of 50% crystallinity, assuming additivity of the crystalline and amorphous regions with respect to the volume[16,17]). Thus, the experimental value of the density is about 0.900 g/cm^3. The corresponding length of Flory segment is 5.51 Å. The value used here for the characteristic ratio (C_∞) is 6.5.[18] On the other hand, the structure of the network is determined using the weighting factors derived at the melt temperature of ~500 K, where the samples were prepared (see experimental work reported in ref 5).

Important interaction parameters of our coarse-grained network model, which we have to specify, are the LJ energy ϵ, the LJ length σ_{LJ}, and the hard-sphere diameter d_{HS}. The well of the LJ potential used to describe attractive interactions between monomer units is attained at a distance of $2^{1/6}\sigma_{\text{LJ}}$. The parameter d_{HS} is the diameter of the hard spheres representing monomer units, used in calculating the repulsive free energy. As a first approximation (in order to minimize the number of parameters) we assume that the two lengths d_{HS} and σ_{LJ} have equal values. Thus, we have to set ϵ and σ_{LJ} so as to reproduce the properties of isotactic PP at room temperature. The cohesive energy density, defined as the increase in energy per volume if all intermolecular forces are eliminated, is estimated as A^{attr}/V_0 at the state of minimum free energy (mechanical equilibrium) of the network. Also, the isothermal compressibility (κ_T) is calculated from the second derivative of the free energy with respect to the volume. The latter is estimated from the minimal values of the free energy attained in specimens fully relaxed at volumes $V_0 - \Delta V$, V_0, and $V_0 + \Delta V$.

$$B = \frac{1}{\kappa_T} = V_0 \left(\frac{\partial^2 A}{\partial V^2} \right)_{V=V_0} = V_0 \frac{A(V_0 + \Delta V) + A(V_0 - \Delta V) - 2A(V_0)}{\Delta V^2} \quad (15)$$

The experimental value[16,17] of the isothermal compressibility is about 3.5 GPa. We have implemented our network generation methodology for samples of bulk isotactic polypropylene of different sizes, all filled with monodisperse chains (600 Flory segments each).

We minimized the free energy of the network specimens according to the algorithm described above, assuming various values of the parameters, in the range 2.0−5.0 Å for σ_{LJ} and in the range $0.10-0.70 k_B T$ for ϵ (T being the temperature, here 300 K). These values are in the range of the parameters used in ref 19 for a more detailed simulation of PP. One should point out, however, that our parameters here refer to entire monomers and not to united atoms (CH_x, $x = 1$, 2, and 3) as in ref 19.

For most values of the parameters examined, the entropy spring free energy did not exceed 10% of the attractive energy. Moreover, for values of the parameter σ in the range 3.5−5.0 Å and independently of the ϵ value, the density distribution in our bulk PP became homogeneous. After extensive investigations we have concluded that best agreement between calculated

Table 1. Densities of Monomers in Cells, before and after Minimization of the Free Energy, for a Bulk Specimen of PP Composed of Monodisperse Chains

	density in cell in g/cm^3	
cell position[b]	before minimization	after minimization
(1,1,1)	0.812	0.891(9%)[c]
(2,5,2)	0.734	0.894(18%)
(3,8,4)	0.934	0.903(4%)
(4,4,1)	0.788	0.896(12%)
(5,5,6)	0.767	0.898(15%)
(6,4,4)	0.911	0.899(1%)
(7,3,10)	0.901	0.911(1%)
(8,7,1)	0.866	0.890(3%)
(9,5,6)	0.799	0.899(11%)
(10,1,9)	0.876	0.899(3%)

[a] The length of each chain is 600 Flory segments (∼54 kg/mol). The number of chains was 1243; the system dimensions in the relaxed state were 500 Å × 500 Å × 500 Å. [b] Results given only for a few cells. Total number of cells is 1000. [c] Percent change in density.

values of the density, cohesive energy and bulk modulus based on our network model and the experimental values for bulk PP is achieved for $\epsilon = 0.43k_BT$ and $\sigma_{LJ} = 3.6$ Å. For these values of the parameters we obtained a relaxed specimen density $\rho = 0.898 \pm 0.002$ g/cm^3, cohesive energy density (attractive interaction/volume of the specimen) $= 290 \pm 40$ J/cm^3, and isothermal compressibility (from introducing 1% change of the volume in either direction, and reminimizing the free energy, according to eq 15) $= 3 \pm 1$ GPa.

The final configuration of the sample is characterized by a uniform density of segments (see Table 1). In addition, we checked if our final equilibrated network configuration exhibits density fluctuations (last column in Table 1) consistent with the estimated bulk modulus. A Gaussian distribution of the number density among the cells was observed. The following relation relates the bulk modulus B, which is the inverse of the isothermal compressibility (κ_T), to the density fluctuations in an equilibrium system:[20]

$$\frac{1}{\kappa_T} = \frac{k_BT}{V_c}\frac{1}{\left(\frac{\Delta\rho}{\bar{\rho}}\right)^2} \tag{16}$$

V_c is the volume of each cell (equal to l_g^3), T is the temperature, $\bar{\rho}$ is the average number density, and $\Delta\rho$ is the density fluctuation, specified by the width (standard deviation) of the Gaussian distribution. The value of the bulk modulus estimated in this way is about 3.2 GPa in excellent agreement with the estimate obtained from the direct small-strain hydrostatic compression−tension calculations reported above. In addition, we have used bulk simulations to estimate the Poisson ratio. The Poisson ratio ν is formally defined as the ratio of the true strain in the transverse direction to the true strain in the longitudinal direction in a uniaxial tension experiment. It can be calculated by the following expression:[21]

$$\nu = \frac{1}{2}\left[1 - \frac{1}{V}\left(\frac{\partial V}{\partial \epsilon}\right)\right] = \frac{1}{2}\left[1 - \frac{1}{V(\epsilon)}\left(\frac{V(\epsilon + \Delta\epsilon) - V(\epsilon)}{\Delta\epsilon}\right)\right], \tag{17}$$

ϵ is the engineering (nominal) strain $(L - L_0)/L_0$, where L_0 is the original (undeformed) sample length and L is the length after the uniaxial tension is imposed. In eq 17, $V(\epsilon)$ is the volume of the relaxed (free energy minimized) specimen at strain ϵ. From our simulations, using ϵ's from 1%−5%, we estimated a Poisson ratio of ∼0.45. From the experimental values[16] of bulk modulus ($B \cong 3.5$ GPa) and shear modulus ($G \cong 0.7$ GPa), using $B = {}^2/_3G[(1 + \nu)/(1 - 2\nu)]$, one obtains $\nu \sim 0.41$, which is reasonably close to, but lower than, our estimated value. Once the Poisson ratio and the bulk modulus (B) are known, one can estimate the Young's modulus using the expression[22] $E = 3(1-2\nu)$B. In this way, we estimated $E_{bulk} = 0.9 \pm 0.3$ GPa, which is comparable to experimental values[16,22] reported for bulk PP, which are in the region between 1.1 and 2GPa.

By performing direct uniaxial tension experiments on bulk PP specimens we estimated $E_{bulk} = 0.7 \pm 0.1$ GPa. Using the relation $E = 3(1-2\nu)B$, this gives $\nu \cong 0.46$.

It is important to point out that our results are insensitive to variations of the cell size l_g, once we have achieved the free energy minimization. We start our minimization procedure with cell size such that in each cell three to eight nodes are included. We decrease the size of each cell gradually. We end up with cells that include on the order of one node each.

Network Deformation. A fully relaxed network is deformed at constant strain rate according to a kinetic Monte Carlo (KMC) algorithm.[7] The strain is imposed in small steps, after each of which the system is allowed to relax to mechanical equilibrium. At each step, microscopic deformation processes that change the topology of the network are allowed to occur. Prominent among these is chain slippage across an entanglement, which is governed by a "Zhurkov-type" activated rate expression[23] depending on the local stress situation around the entanglement. Following the KMC simulation of elementary deformation events, the system is allowed to relax anew to mechanical equilibrium. A new incremental strain is then imposed and the cycle is repeated, until the specimen breaks (see Figure 4).

The micromechanisms allowed in the simulation of deformation are translation of entanglements and end points in space, which occurs simply in the course of minimization of the free energy, chain slippage across an entanglement, chain disentanglement, chain reentanglement, and chain scission.[7] The procedure used to implement the latter four processes is described below.

•Chain slippage corresponds to motion of an entanglement point along the contour of a chain without displacement of the entanglement point in space (Figure 5). Two of the four strands emanating from an entanglement are involved in a slippage event. One strand increases in length by a Kuhn segment and the other decreases by the same length. The difference in force experienced by the two strands involved acts to decrease the activation energy for changing the strands in a direction that relieves the force differential. The rate constant of an elementary slippage event is given by an equation similar to the one invoked in ref 7:

$$k_{slip} = k_0 \exp\left[-\frac{E^* - l_K\Delta F_{slip}}{k_BT}\right]. \tag{18}$$

The required parameters E^* and k_0 are estimated following a procedure that will be described in the next paragraph. To calculate the driving force for slippage, ΔF_{slip}, we have to calculate the forces on the central entanglement point due to each of the two strands that are involved. The total (entropy spring, repulsive, and attractive) force due to a specific strand is computed

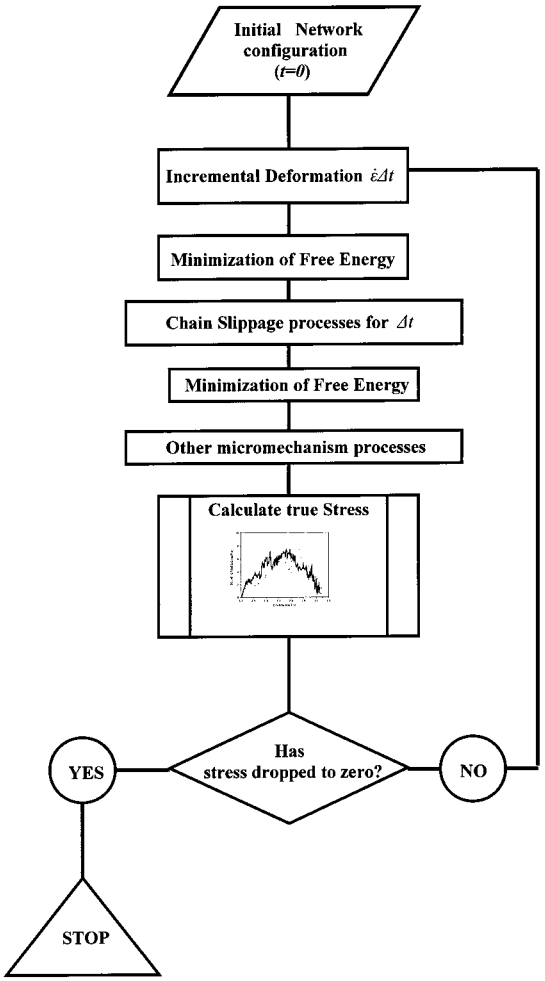

Figure 4. Logical diagram of the deformation simulation algorithm. By "other micromechanism processes", we mean disentanglement, reentanglement, and rupture of bonds.

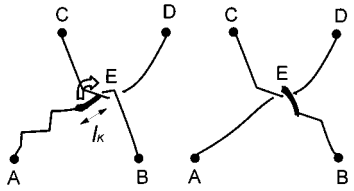

Figure 5. Schematic representation of chain slippage. Spheres represent nodes (end points or entanglements) and chain strands are represented by curvilinear segments. Slippage occurs along the direction specified by the arrow (left-hand side figure). After slippage, the strand AE is shorter by one Kuhn segment and the strand EB is longer by one Kuhn segment (right-hand side figure). The top chain strands (CE, ED) do not change contour length or number of segments during chain slippage. The sphere corresponding to the entanglement point (E) between the top and the bottom chains, across which slippage occurs, has been omitted for clarity. The position of the entanglement point remains unchanged.

from the derivative of the free energy with respect to the coordinates of the entanglement point (eqs 13 and 14), assuming that the infinitesimal displacement of the entanglement point affects only the specific strand. The direction of the force is generally not parallel to the strand (treated as linear segment); only the entropy spring force always acts along the strand. The slippage force, ΔF_{slip}, is the projection along the tangent of the slipping chain of the total force on the entanglement point due to the two adjacent strands (see Figure 6).

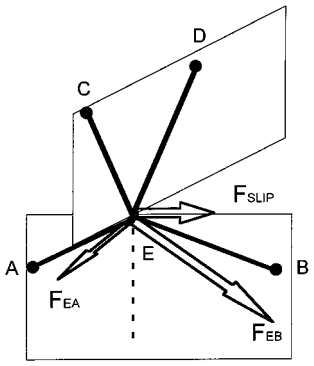

Figure 6. Schematic representation of slippage force, $\vec{F}_{\text{slip}}$, on the chain segment AEB defined as the component, along the tangent to the chain at E, of the total force acting on the entanglement E due to the two adjacent strands EA and EB. In this figure, linear segments represent strands. The slippage force lies in the plane AEB, defined by the slipping strands, in a direction normal to the bisector of angle AEB. As in Figure 5, the sphere corresponding to the central entanglement point has been omitted for clarity.

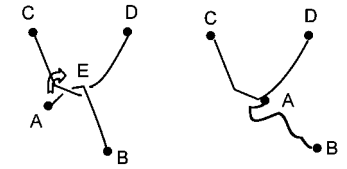

Figure 7. Schematic representation of chain disentanglement. Nodal point A of chain AEB is a chain end. Strand AE of chain AEB is one Kuhn segment long or less. Slippage of AEB in the indicated direction leads to elimination of entanglement point E. After chain disentanglement, the number of entanglement points in the network decreases by one and the number of strands by two.

•Chain disentanglement occurs when chain slippage allows an end to slip past an entanglement point (Figure 7). A reverse, reentanglement process occurs when two strands attempt to pass through each other. Free end strands and interior strands may reentangle with other strands to form new entanglement points. The tracking of reentanglements is implemented on a purely geometric basis by examining all pairs of strands at close distances. Strands reentangle as a result of node displacements after the end of each minimization procedure. Initially (just before minimization), we form the shortest distance (common perpendicular vector) between a pair of neighboring strands, envisioned as rectilinear segments. After minimization, we reform the distance vector and check for distance vectors that have reversed their direction. Direction reversal signals that a reentanglement has occurred. The new entanglement point is taken as the point where the rectilinear segments representing the strands intersected (practically, as the midpoint of the distance vector after minimization; see Figure 8). A similar procedure has been used by Padding and Briels[24] to track entanglements in the course of dynamic simulations of polymer melts.

•When a strand is stretched to its contour length, the strand is assumed to break. Chain scission entails breaking of a covalent bond along the backbone of the chain, because the tensile force along the chain overcomes the force holding the bond together. When the strand is overstretched, all the bonds along the chain feel the same force. Consequently, the position for the breaking bond is chosen randomly along the strand contour. A chain scission event generates two new end points in the network.

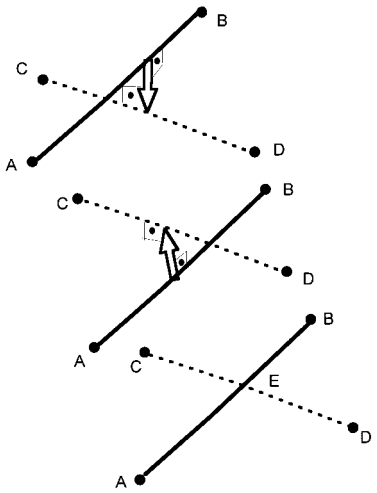

Figure 8. Schematic representation of chain reentanglement. If, in the course of the displacement of nodal points A, B, C, and D the minimum distance vector between the strands CD and AB, represented as linear segments, changes direction, chain reentanglement (emergence of a new entanglement point E) takes place.

Kinetic Monte Carlo Algorithm. The deformation entails three basic types of computation: straining of the system, relaxation to mechanical equilibrium, and KMC sampling of the micromechanisms (see Figure 4).

The initial system configuration is a relaxed, undeformed network (free energy A at a local minimum). An incremental strain is imposed on the boundaries at each step. The incremental strain imposed is equal to the constant strain rate times the time increment (Δt). In imposing the incremental strain, a large section of the top boundary elements is held rigid ("clamped" region, see Figure 9). The size of the "clamped" region is chosen such that each free chain has at least one entanglement point in this region. Its width is approximately equal to the radius of gyration of the free chains. In introducing the small strain, all interior nodes of the network are displaced affinely in the z-direction, normal to the interface.

After the incremental strain is imposed, the network is allowed to relax to mechanical equilibrium by minimizing the free energy A. The resulting relaxed network configuration is not affinely deformed, since the chain strands are not all of the same length and fluctuations in density induce local inhomogeneities in attractive and repulsive forces. After relaxing to mechanical equilibrium, and for a time Δt, the elementary processes (micromechanisms) modifying the network topology are allowed to occur in parallel.

As in our model of elementary micromechanical events we have only one process (chain slippage) which is described by an activated rate expression, the deformation simulation is performed for fixed $\tilde{k}_0\,\Delta t$ ($\tilde{k}_0 = k_0 e^{-E^*/kT}$, k_0 being the frequency factor and E^* the activation energy for slippage), i.e., using $1/\tilde{k}_0$ as the unit of time. This means that $\dot{\epsilon}/\tilde{k}_0$, rather than $\dot{\epsilon}$, is actually set in the simulation. Then the number of slippage events expected to occur for a specific pair of strands across a specific entanglement point within the time interval Δt is given by $\tilde{k}_0\,\Delta t\, e^{-l_K \Delta F_{\mathrm{slip},i}/k_B T}$, where index i designates the particular pair of strands and entanglement point considered. The total number of slippage events expected to occur within the interval Δt is $\tilde{k}_0\,\Delta t$ ($\sum_i e^{-l_K \Delta F_{\mathrm{slip},i}/k_B T}$) (Poisson process). The probability that a *particular* slippage event i will occur is

$$p_i = \frac{e^{-l_K \Delta F_{\mathrm{slip},i}/k_B T}}{\sum_i e^{-l_K \Delta F_{\mathrm{slip},i}/k_B T}} \tag{19}$$

In our simulation we first determine the total number of events to occur in the current step and then pick the particular events according to $\{p_i\}$. Moreover, the disentanglement, reentanglement, and rupture events are introduced after the simulation of slippage (second minimization). By repeating this series of stepwise calculations many times, we produce stress−strain curves. The engineering stress is calculated from the total force on the nodal points contained in the "clamped" region (which is practically identical to the force on the PA6 substrate).

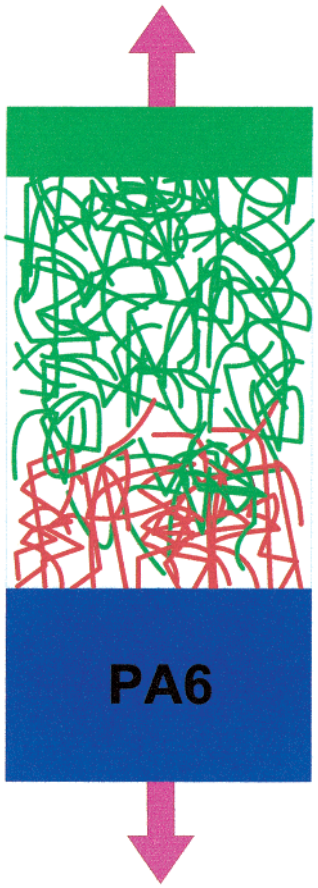

Figure 9. Tensile deformation imposed on a macroscopic PP/PA6 sample at constant strain rate $\dot{\epsilon}$. Grafted chains are represented in red color and free chains in green. At the bottom, the specimen is physically clamped by the "solid" PA6.

Parameters for Deformation Simulation. An estimation of the slippage rate parameters E^* and k_0 is necessary in order to set the absolute time scale of our computer experiments. We can arrive at these estimates as follows:

If we consider a very weak driving force (i.e. $l_K \Delta F/k_B T \ll 1$), the slippage rate becomes

$$k_{\mathrm{slip}} = k_0 \exp\left[-\frac{E^* - l_K \Delta F_{\mathrm{slip}}}{k_B T}\right] \approx k_0 \exp\left[-\frac{E^*}{k_B T}\right]\left[1 + \frac{l_K \Delta F_{\mathrm{slip}}}{k_B T}\right] = k_{\mathrm{diff}} + k_{\mathrm{drag}} \tag{20}$$

The term $k_{diff}(\equiv k_0 \exp[-(E^*/k_BT)])$ is related to the self-diffusion along the contour of the chain (i.e., it estimates the rate for slippage in both directions along the contour due to random forces, which are present even at equilibrium). The second term $k_{drag}(\equiv k_0 \exp[-(E^*/k_BT)] \cdot (l_K \Delta F_{slip})/(k_BT))$ is related to the force-induced dragging of chain segments in a linear regime, where the slippage rate is proportional to the driving force. k_{diff} and k_{drag} can be related directly to the Rouse-reptation picture of polymer dynamics (see Appendix A). By matching the Rouse self-diffusivity of the chain along its contour with k_{diff}, we obtain the following expression: $\rho/(36M_0)\ [RT/(\eta/N)_{unentangled}] = k_0 \exp[-E^*/k_BT]$, where ρ is the mass density, M_0 the molecular weight of each Kuhn statistical segment, N the number of Kuhn segments per chain in an unentangled melt, and η the melt viscosity at the prevailing temperature. Exactly the same expression is obtained by matching k_{drag} to the Rouse friction coefficient, ζ (see Appendix A). To estimate the activation energy (E^*) and thermal vibration frequency (k_0), we need a model to describe the temperature dependence of the viscosity (η). The procedure followed for this is described in Appendix B. The time interval (Δt) can either be chosen fixed, or it can vary as the simulation progresses. In both cases, the following relation can be used to pick an appropriate Δt for the KMC simulation: $\Delta t \propto k_0 \max_i \{\exp[-l_K \Delta F_{slip,i}/(k_BT)]\}$ where index i runs over all pairs of successive strands at all entanglement points in the system. By testing the constant Δt and the variable Δt approach against each other, we have concluded that the results are very similar. We use the constant time interval approach, as it is more convenient.

3. Results

Mechanical Properties. In the study of the PP/PA6 interfacial system we assume that the energy parameters of the PP phase (ϵ and σ_{LJ}) have the same values as the ones extracted from our calculations of density, cohesive energy density, and small strain mechanical response of bulk PP. Assuming a generalized WLF-type expression for the viscosity (eq B4) with parameters from ref 16, we derive estimates for the slippage activation energy E^* and for the frequency of thermal vibrations k_0. As explained in detail in Appendix B, the literature values for PP properties we invoked as input for the KMC simulation are: glass transition temperature $T_g = 253$ K, activation energy for viscosity $E_\eta(\infty) = 44$ kJ/mol and critical molecular weight for entanglements, based on viscosity, $M_{cr} = 7$ kg/mol. The molecular weight of a Kuhn segment is 0.174 kg/mol (derived from $M_0 = [l_K/(2l_b\ sin(\theta_b/2))]M_m$, where M_m is the molecular weight of PP monomers, $l_b = 1.54$ Å is the skeletal bond length, and $\theta_b = 112°$ is the skeletal bond angle). The parameter values derived and used in the present work are $E^* = 11.2$ kcal/mol for the slippage activation energy and $k_0 = 4.8 \times 10^{12}$ s^{-1} for the frequency factor. A value of 10^{12} s^{-1} is usually assumed a priori for k_0; see refs 7 and 15. For comparison, the E^* value used in ref 7 for polyethylene was 20 kcal/mol.

The time interval (Δt) was set at 0.001 s. We mainly report the true stress, defined as the ratio of measured force to the actual cross sectional area ($\tau = F/S$, F force, and S cross sectional area). The engineering (nominal) stress τ_E is defined using the cross sectional area of the undeformed specimen S_0. As in our simulations the cross-section varies through out the specimen, we have computed S as the average cross section, i.e., as the ratio of the total volume to the height of the specimen.

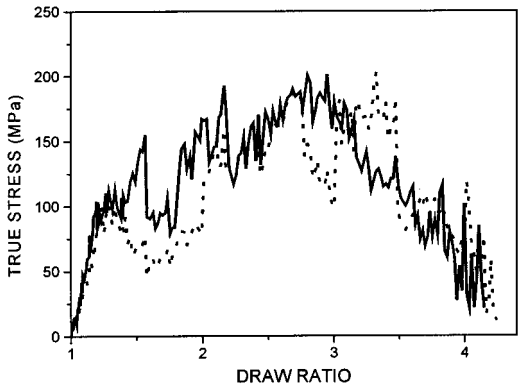

Figure 10. True stress−draw ratio curves for sample with $M_n^g = 40$ kg/mol (molecular weight of grafted PP chains) and $M_n^f = 60$ kg/mol (molecular weight of free PP chains), both grafted and free chains being monodisperse. The size of the sample is 45 nm × 45 nm × 70 nm, the total number of chains is 1300, and the surface density of grafted chains is 0.10 nm^{-2}. The dotted line corresponds to a deformation at strain rate 1% per second and the solid line corresponds to a deformation at strain rate 10% per second.

Figure 10 shows the true stress−strain curves that were calculated from deforming an interfacial specimen at two different strain rates ($\dot{\lambda}$, namely 1% and 10% per second based on the initial height of the specimen). The draw ratio λ ($\lambda \equiv 1 + \epsilon$) is used as the abscissa. The network consists of monodisperse grafted chains of molecular weight 40 kg/mol and monodisperse free chains of molecular weight 60 kg/mol. The size of the specimen in the undeformed state is 450 Å × 450 Å × 700 Å, the total number of chains is 1300 and the surface density of grafted chains is 0.10 nm^{-2}. A stress−strain behavior typical of semicrystalline polymeric systems is observed. Initially, the stress−strain curve displays a linear (elastic) region. One can estimate a Young's modulus for the interfacial specimen as $E = (\partial\tau/\partial\lambda)_{\lambda=1}$. In this way, an apparent Young's modulus for the PP/PA6 interfacial specimen is estimated (from Figure 10) as about 0.49 GPa, which is smaller by roughly a factor of 2 than the moduli usually reported for bulk polymers (see refs 16, 17, 22, and 25) and then the value found in our bulk PP simulations (∼0.7 GPa). At larger elongations, the stress−strain curve of Figure 10 shows a yield point (first maximum in the stress−strain curve, $\lambda \sim 1.3$). Beyond the yield point, a strain hardening region sets in. The overall drawability of the material is rather high and the sample breaks at a high draw ratio (i.e., about 2.95). From the same figure, it is observed that the stress−strain curve obtained by applying higher strain rate shows more strain hardening and breakage at a lower draw ratio. From the point of view of the simulations, this is expected, as higher rate elevates the yield stress. This is also in agreement with experimental results.[26] If we compare Figures 10 and 11, where the surface density of the grafted chains is different ($\sigma = 0.40$ nm^{-2}), we observe that the sample with $\sigma = 0.10$ nm^{-2} is more drawable. This is in accordance to what was predicted in our previous paper (ref 2), where a maximum of the adhesion was expected for $\sigma = 0.10$ nm^{-2}. Careful examination of the results leads to the following insight and rationale for the observed behavior and for the marked differences in the stress−strain behavior between the two samples. The initial linear region corresponds to the elastic behavior.

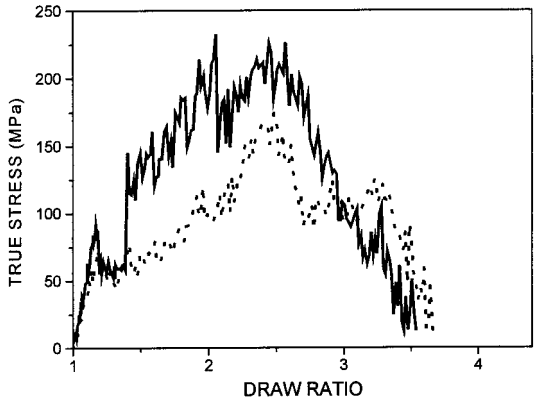

Figure 11. True stress−draw ratio curves for sample as in Figure 10, but here the total number of chains is 1600 and the surface density of grafted chains is 0.40 nm^{-2}. The size of the sample is 45 nm × 45 nm × 70 nm. The dotted line corresponds to a deformation at strain rate at 1% per second, and the solid line corresponds to a deformation at 10% per second.

It occurs for low values of elongation (less than 20%). In this regime, there is no breaking of bonds, and there is very little chain slippage. The strands are mainly behaving as elastic springs, with entanglement nodes redistributed upon deformation almost affinely. In addition, in this region an almost uniform distribution of the local stresses is expected. As we increase the strain (at constant strain rate) the linear behavior terminates at the yield point. Now there is no affine response to incremental increase of the sample length. Bond rupture, chain slippage, chain disentanglement, and chain reentanglement are contributing significantly. There may be local regions of high stress due to the existence of strands of unequal length (shorter chain segments). The drawing region and the strain hardening region are dominated by the chain slippage process. To confirm this we have performed exploratory calculations, assuming that the slippage process is not present. We have observed (not shown here) a much less drawable behavior of the sample with a much sharper strain−hardening effect. Finally, there is a region, beyond the maximum in τ, where the sample shows a constant decrease of the stress until the specimen is separated in two. In this region we mainly have breaking of the bonds and chain disentanglements. Once some bonds break, the local stress in the vicinity increases, which results in an increase in the bond breaking and slippage of the other strands. Visual observation of our specimens reveals that fracture occurs at the interfacial region, where grafted and free chains interpenetrate (see Figure 12). The last observation explains why the specimen of the small surface grafting density[1] (σ = 0.10 nm^{-2}) is more difficult to break compared to the sample of modest surface grafting density (σ = 0.40 nm^{-2}). As shown in our previous work, the number of entanglements between grafted and free chains goes through a maximum at σ = 0.10 nm^{-2}, and therefore optimal adhesion is expected at this surface grafting density (refs 1 and 2). By running simulations with different initial configurations, we have shown that stress−strain curves are quite reproducible. The effects of changing the molecular weight and its distribution are currently under investigation. Preliminary results reveal a terminal mechanical behavior in agreement with what is expected from the structural results reported in refs 1 and 2.

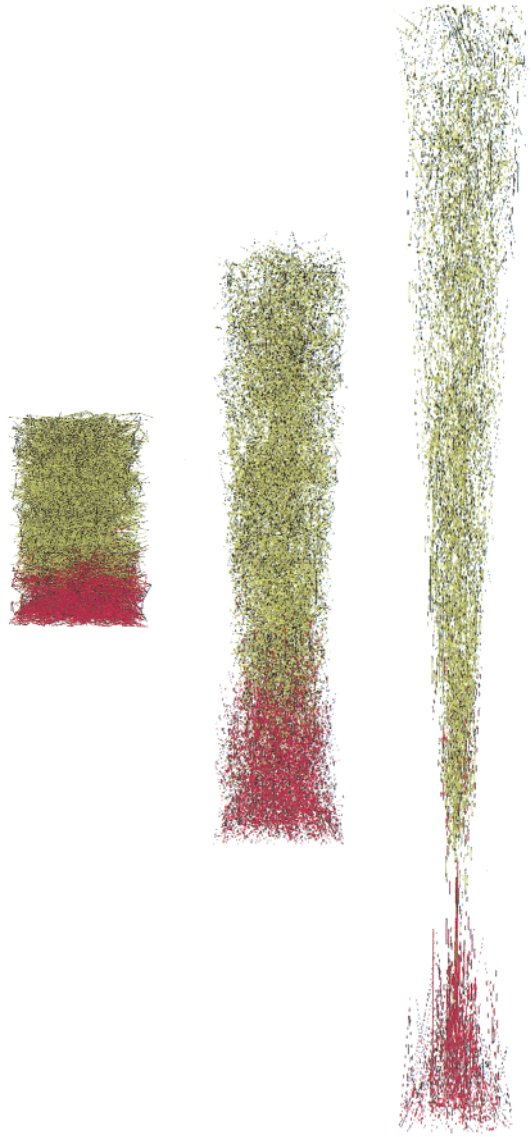

Figure 12. Three-dimensional visualization of an entanglement network with M_n^g = 40 kg/mol and M_n^f = 60 kg/mol (both monodisperse) and with low surface density of the grafted chains (σ = 0.10 nm^{-2}). Strands are represented as rods. Grafted chains are represented in red color and free chains in green. The specimen consists of 1300 grafted and free chains (45 nm × 45 nm × 70 nm): (a) generated network after free energy minimization (relaxed network); (b) same network at draw ratio of 2.5; (c) network at a draw ratio of 4.0, after fracture has occurred.

4. Conclusions

The present study and the work reported in refs 1 and 2 embody simulation efforts aimed at establishing links between different levels of description, and thereby addressing different windows of time and length scales in the terminal mechanical behavior of interfacial systems containing polymers. Each level of modeling receives input from more fundamental levels and provides input to more coarse-grained ones. Our present work concerned modeling structure and adhesion at polymer/solid interfaces strengthened with block copolymers. The first step in this approach was to estimate the compositional and conformational profiles of all macromolecular species present in the interfacial region using a lattice-based self-consistent field model (see ref 1). In the second step, entanglement networks are generated using the structural information derived in

the first step (see ref 2). In the third step (present work), a numerical technique is developed for minimizing the free energy of a network specimen with respect to the positions of all nodal points (chain ends and entanglement points). The coarse-grained free energy of the network incorporates excluded volume, dispersion attraction, and entropy spring terms. Furthermore, a kinetic Monte Carlo scheme is developed and applied at prescribed temperature and strain rate in order to deform our network until fracture occurs.

In the present work we have shown the following: (a) It is possible to mechanically relax coarse-grained network specimens of solid polymers by minimizing a numerically estimated free energy. Samples of uniform density, exhibiting density fluctuations consistent with their isothermal compressibility, are generated through this procedure. (b) We can parametrize the coarse-grained free energy function using experimental density, cohesive energy, and elastic constant data. Furthermore, we can parametrize the rate expression for elementary slippage events in the network using experimental viscosity data, and all parametrizations lead to consistent and physically reasonable values. (c) We can apply a tensile stress perpendicular to the interface and hence deform a coarse-grained interfacial specimen at constant strain rate, taking into account elementary mechanical processes such as chain scission, chain slippage, disentanglement, and reentanglement until breakage occurs. (d) We can use the results of such simulations of highly irreversible deformation processes to identify optimal molecular design characteristics, e.g., the surface grafting density that maximizes the work required for interfacial fracture.

Simulating the deformation process is rather demanding in CPU time. To produce the true stress−draw ratio curve shown in Figure 10 at strain rate 1% we need four to five weeks CPU time on a single-processor SGI R10000 180 MHz workstation. The degree of difficulty increases with the polydispersity index. In the present work we have presented results on monodisperse specimens. In ref 2, we have shown that a maximum is observed in the number of entanglements between grafted and free chains per unit area of the interface for an optimal surface density of grafted chains. In our present study, best adhesion is observed at similar values of the surface density of grafted chains.

In conclusion, one can say that the observed results are in good agreement with both available experimental evidence and predictions from our previous work. Moreover, the procedure followed in this work in order to track deformation to fracture of an entanglement network is rather general; it can easily be applied to polymeric systems of different chemical constitution and topology.

Acknowledgment. Computational resources for this research were made available by the Educational and Initial Vocational Training Program on Polymer Science and Technology—3.2a. 33H6. A.F.T. is grateful to DSM Research for financial support.

Appendix A

The first term of eq 19 ($k_{diff} \equiv k_0 \exp[-E^*/k_BT]$) is related to self-diffusion along the contour of the chain. To get an expression for this self-diffusive term, we describe self-diffusion along the chain contour with the Rouse model.[27] The Rouse model addresses the dynamics of polymers in an unentangled melt. A polymer chain is represented by a set of beads connected by harmonic springs. The dynamics is modeled as a Brownian motion of these tethered beads, the environment of a chain being represented as a continuum (viscous medium), ignoring all excluded volume and hydrodynamic interactions. The central assumption in the Rouse model is that the dynamics is governed exclusively by *local* interactions along the chain. In this model the self-diffusion of the center of the mass of the polymer is related to the friction constant (ζ) on a bead by

$$D_{\text{Rouse}} = \frac{k_B T}{N\zeta} \tag{A1}$$

N being the number of beads per chain.

The longest relaxation time, τ_1, corresponding to the time needed for the chain to travel a distance comparable to its size, is estimated by

$$\tau_1 = \frac{\zeta N^2 b^2}{3\pi^2 k_B T} \tag{A2}$$

where b can be identified with the Kuhn segment length l_K.

Relaxation times are useful for studying viscoelastic properties of polymers. In the context of Rouse model, from τ_1 and other shorter relaxation times, we derive an expression for the viscosity of unentangled melts[27]

$$\eta = \frac{\rho b^2 N N_A \zeta}{36 M_0} \tag{A3}$$

ρ being the mass density, N_A being the Avogadro number, and M_0 being the molecular weight of a Kuhn statistical unit.

By combining eqs A1 and A3, we get an expression for the Rouse diffusivity in terms of the viscosity:

$$D_{\text{Rouse}} = \frac{\rho b^2}{36 M_0}\left(\frac{RT}{\eta/N}\right)_{\text{unentangled}}\frac{1}{N} \tag{A4}$$

Equation A1 and therefore eq A4 continue to describe diffusivity along the contour (primitive path) in a long-chain, entangled polymer melt (reptation model[27]). In the picture we invoke in our network model, the center of mass diffusivity along the contour is related to the rate of jumps across entanglements (by distance l_K) in each direction by

$$D_{\text{Rouse}} = k_{\text{diff}}\frac{{l_K}^2}{N} \tag{A5}$$

Hence, one must have

$$\frac{\rho b^2}{36 M_0}\left(\frac{RT}{\eta/N}\right)_{\text{unentangled}} = k_0 {l_K}^2 \exp\left[-\frac{E^*}{k_B T}\right] \tag{A6}$$

The second term of eq 19 ($k_{drag} \equiv k_0 \exp[-E^*/k_BT]\cdot(l_K\Delta F_{slip})/k_BT$) is related to the force-induced dragging of the chain. In this case the drag force is proportional to velocity of motion of a segment through the rest. We typically use a phenomenological law for the motion of a segment:

$$\zeta u_{\text{drag}} = \Delta F_{\text{slip}} \tag{A7}$$

u_{drag} is the velocity at which the segment is dragged, and $\Delta F_{slip}$is the driving force.

In our model

$$u_{drag} = k_{drag} l_K \tag{A8}$$

and by combining with eq A3 and eq A7, we get

$$\frac{\rho b^2}{36 M_0}\left(\frac{RT}{\eta/N}\right)_{unentangled} = k_0 {l_K}^2 \exp\left[-\frac{E^*}{k_B T}\right] \tag{A9}$$

It becomes clear from eqs A6 and A9, that "diffusion" and "dragging" pictures lead to exactly the same result. If one chooses $b = l_K$ (as is done in this work), then both eqs A6 and A9 simplify to

$$\frac{\rho}{36 M_0}\left(\frac{RT}{\eta/N}\right)_{unentangled} = k_0 \exp\left[-\frac{E^*}{k_B T}\right] \tag{A10}$$

with $(\eta/N)_{unentangled}$ being molecular-weight independent in the Rouse regime.

Appendix B

To estimate activation energy (E^*) and thermal vibration frequency (k_0), we need a model to describe the temperature dependence of the viscosity (η). The melt viscosity depends on molecular weight (M) and temperature (T). There are no cross-terms between the dependencies of η on M and T, however the M dependence of η has the same functional form, regardless of the value of T. The T dependence of η has the same functional form regardless of the value of M. In the Rouse (unentangled) regime we usually write[25]

$$\eta(T,M) \approx \eta_{cr}(T)\left(\frac{M}{M_{cr}}\right) \tag{B1}$$

where M_{cr} is an intrinsic property of a polymer called the critical molecular weight.

For molecular weight M larger than M_{cr}, the functional form of the dependence of η on M changes to

$$\eta(T,M) \approx \eta_{cr}(T)\left(\frac{M}{M_{cr}}\right)^{3.4} \tag{B2}$$

A Williams−Landel−Ferry (WLF) model[28] is usually invoked in order to give a fair description of the effect of temperature on viscosity (η):

$$\log\left(\frac{\eta}{\eta_{T_g}}\right) = \frac{-C_1(T - T_g)}{C_2 + (T - T_g)} \tag{B3}$$

T_g is the glass temperature and C_1 and C_2 universal constants[16,17] or constants estimated from experimental data. According to eq B3, η/η_{T_g} should be a universal function of $(T - T_g)$, which is not confirmed by experimental data. Van Krevelen[16,25] has proposed a revised viscosity−temperature relationship, which satisfies an Arrhenius-type equation for high temperatures and corresponds to a WLF-type relationship in the neighborhood of T_g.

The general formula of this description is

$$\log \frac{\eta_{cr}(T)}{\eta_{cr}(1.2T_g)} = A\left(\frac{T_g}{T} - 1\right) \tag{B4}$$

If the glass temperature is known, we estimate $\eta_{cr}(T)$ by

$$\log \eta_{cr}(T_g) = E_\eta(\infty)\left(\frac{0.052 - (8.5 \times 10^{-5})T_g}{T_g}\right) - 1.4 \tag{B5}$$

A and $E_\eta(\infty)$ are related by the following equation:[16]

$$A = \frac{E_\eta(\infty)}{2.3RT_g} \tag{B6}$$

The rhs of eq A10 can be rewritten as

$$\frac{\rho}{36 M_0}\left(\frac{RT}{\eta(T,M)/N}\right) = \frac{\rho M_{cr}}{36 {M_0}^2}\left(\frac{RT}{\eta_{cr}(T)}\right) = \left(\frac{M_{cr}\rho R}{36\, {M_0}^2 \eta_{cr}(1.2T_g)}\right) T\, e^{-(A/\log e)[(T_g/T)-1]} \tag{B7}$$

To derive the above expression we have used eq B1. M ($\equiv NM_0$) is the molecular weight of the chain composed of N Kuhn segments (M should be smaller than M_{cr} in order to use eq B1).

References and Notes

(1) Terzis, A. F.; Theodorou, D. N.; Stroeks, A. *Macromolecules* **2000**, *33*, 1385.
(2) Terzis, A. F.; Theodorou, D. N.; Stroeks, A. *Macromolecules* **2000**, *33*, 1396.
(3) (a) Creton, C.; Kramer, E. J.; Hui, C.-Y.; Brown, H. R. *Macromolecules* **1992**, *25*, 3075. (b) Washiyama, J.; Creton, C.; Kramer, E. J. *Macromolecules* **1992**, *25*, 4751. (c) Washiyama, J.; Kramer, E. J.; Creton, C. F.; Hui, C.-Y. *Macromolecules* **1994**, *27*, 2019.
(4) Cho, K.; Li, F. *Macromolecules* **1998**, *31*, 7495.
(5) Boucher, E.; Folkers, J. P.; Hervet, H.; Leger, L.; Creton, C. *Macromolecules* **1996**, *29*, 774.
(6) Boucher, E.; Folkers, J. P.; Creton, C.; Hervet, H.; Leger, L. *Macromolecules* **1997**, *30*, 2102.
(7) (a) Termonia, Y.; Meakin, P.; Smith, P. *Macromolecules* **1986**, *19*, 154. (b) Termonia, Y.; Smith, P. *Macromolecules* **1987**, *20*, 835. (c) Termonia, Y.; Smith, P. *Macromolecules* **1988**, *21*, 1284.
(8) Fischel, L. B.; Newman, J.; Theodorou, D. J. *J. Chem. Soc., Faraday Trans.* **1997**, *93*, 4355.
(9) Madras, N.; Sokal, A. D. *J. Stat. Phys.* **1988**, *51*, 561.
(10) Binder, K. *Monte Carlo and Molecular Dynamics Simulations in Polymer Science*; Oxford University Press: Oxford, England, 1995.
(11) Volkenstein, M. V. *Configurational Statistics of Polymer Chains*; Interscience: New York, 1963.
(12) de Gennes, J. P. *Scaling concepts in Polymer Science*; Oxford University Press: Oxford, England 1995.
(13) Hiemenz, Paul C. *Principles of Colloid and Surface Chemistry*; Marcel Dekker Inc.: New York, 1977.
(14) Press, W. H.; Teukolsky, S. A.; Vetterling, W. T.; Flannery, B. P. *Numerical Recipes in Fortran 77, The Art of Scientific Computing*; Cambridge University Press: New York, 1992.
(15) Bicerano, J.; Grant, N. K.; Seitz, J. T.; Pant, K. *J. Polym. Sci., Part B: Polym. Phys.* **1997**, *35*, 2715.
(16) Van Krevelen, D. W. *Properties of Polymers*; Elsevier Science B.V.: Amsterdam, 1997.
(17) Mark, J. E. *Physical Properties of Polymers Handbook*; American Institute of Physics Press: New York, 1996.
(18) In Boyd, R. H.; Philips. P. J. *The Science of Polymer Molecules*; Cambridge University Press: London, 1993; chapter 7.6.3 (Characteristic ratios of polypropylenes), a value of 5.7 is listed for a temperature of 145 °C. This value was actually used in our structure generation calculations (refs 1 and 2), which referred to the molten state. Using the approximate value for $\{\partial(\ln C_\infty)\}/\{\partial T\}$ derived in Mattice et al. (Mattice, W. L.; Suter, U. W. *Conformational Theory of large molecules*; John Wiley & Sons: New York, 1994), a value of ~6 is derived for room temperature. On the other hand, Zirkel et al. (Zirkel, A.; Urban, V.; Richter, D.; Fetters, L. J.; Huang, T. S.;

Kampmann, R.; Hadjichristidis, N. *Macromolecules*, **1992**, *25*, 6148) report a value of 6.2 from both Θ-solvent chain dimension and melt-based SANS measurements on iPP. On the basis of the latter value, C_∞ should be larger than 6.2 at room temperature. In the present work, we use an estimate of ∼6.5 for a room-temperature simulation.

(19) (a)Curro, J. G.; Honnell, K. G.; McCoy, J. D. *Macromolecules*, **1997**, *30*, 145. (b) Curro, J. G.; Weinhold, J. D.; Rajasekaran, J. J.; Habenschuss, A.; Londono, J. D.; Honeycutt, J. D. *Macromolecules* **1997**, *30*, 6264. (c)McCoy, J. D.; Curro, J. G. *Macromolecules* **1998**, *31*, 9362.

(20) Huang, K. *Statistical Mechanics*; John Wiley and Sons Inc: New York, 1963.

(21) Fried, J. R. *Polymer Science and Technology*, Prentice Hall: Upper Saddle River, NJ, 1995.

(22) Dowling, N. E. *Mechanical Behavior of Materials*, Prentice Hall: Upper Saddle River, NJ., 1999.

(23) Zhurkov; S. N.; Korsukov, V. E. *J. Polym. Sci., Polym. Phys. Ed.* **1974**, *12*, 385.

(24) Padding, J. T.; Briels, W. J. *J. Chem. Phys.* **2001**, *115*, 2846.

(25) Bicerano, J. *Prediction of Polymer Properties*; Marcel Dekker: New York, 1993.

(26) Cahn, R. W.; Haasen, P.; Kramer, E. J. *Materials Science and Technology, A Comprehensive Treatment*; VCH: New York, 1993; Vol. 18, Processing of Polymers.

(27) Doi, M.; Edwards, S. F. *The Theory of Polymer Dynamics*, Oxford University Press: New York, 1986.

(28) Williams, M. L.; Landel, R. F.; Ferry, D. J. *J. Am. Chem. Soc.* **1955**, *77*, 3701.

MA010691Z